Advances in Computational Design, *Vol. 9, No. 3 (2024) 213-227*
https://doi.org/10.12989/acd.2024.9.3.213

Developing a framework to integrate convolution quadrature time-domain boundary element method and image-based finite element method for 2-D elastodynamics

Takahiro Saitoh* and Satoshi Toyoda[a]

Department of Civil and Environmental Engineering, Gunma University,
1-5-1, Tenjin, Kiryu, Gunma 376-8515, Japan

(Received March 13, 2024, Revised June 30, 2024, Accepted September 11, 2024)

Abstract. In this study, a framework for coupling of the convolution quadrature time-domain boundary element method (CQBEM) and image-based finite element method (IMFEM) is presented for 2-D elastic wave propagation. This coupling method has three advantages: 1) the finite element modeling for heterogeneous areas can be performed without difficulties by using digital data for the analysis model, 2) wave propagation in an infinite domain can be calculated with high accuracy by using the CQBEM, and 3) a small time-step size can be used. In general, a small time-step size cannot be used in the classical time-domain boundary element method. However, the CQBEM used in this analysis can address a small time-step size. This makes it possible to couple the CQBEM and image-based FEM which require a small-time step size. In this study, the formulation and validation of the pro-posed method are described and confirmed by solving fundamental elastic wave scattering problems. As a numerical example, elastic wave scattering in inhomogeneous media is demonstrated using the proposed coupling method.

Keywords: convolution quadrature method; convolution quadrature time-domain boundary element method (CQBEM); finite element method (FEM); image-based modeling; 2-D elastodynamics

1. Introduction

Recently, the convolution quadrature time-domain boundary element method (CQBEM) has been developed and applied to several engineering problems, such as scalar, viscoelastic, and anisotropic wave propagation (Schanz and Antes 1997, Abreu *et al*. 2003, Saitoh 2024), in an infinite space. In the CQBEM formulation, the convolution quadrature method (CQM), first proposed by Lubich (1998), is applied to the time-discretization convolutions of the time-domain boundary integral equations. The CQM is an accurate and stable numerical approximation technique for convolution integrals. Therefore, the CQBEM can produce high precision solutions if a small time-step size is used. The classical time-domain boundary element method (BEM) (Mansur and Brebbia 1983, Beskos 1987) does not exhibit these superior characteristics. In addition, the CQBEM can deal with infinite regions without any modifications and requires a

---

*Corresponding author, Ph.D., Associate Professor, E-mail: t-saitoh@gunma-u.ac.jp
[b] Master student, E-mail: 180c063@gunma-u.ac.jp

http://www.techno-press.org/?journal=acd&subpage=7 ISSN: 2383-8477 (Print), 2466-0523 (Online)

spatial discretization of the analysis domain as well as the classical one. On the other hand, the finite element method (FEM) (Hughes 1987, Shaw and Andrawes 2017, Azqandi *et al*. 2019) is resistant to nonlinear problems and the de facto standard of the computational methods. For example, image-based modeling (Terada *et al*. 1997, Chung *et al*. 2015) converts the pixel data of a digital image into a finite element mesh and significantly facilitate the modeling phase, greatly enhancing the versatility of the FEM. Image-based modeling has been used for the elastodynamic finite integration technique (EFIT) (Fellinger *et al*. 1995, Nakahata *et al*. 2009), which is an improved version of the finite-difference time-domain method (FDTD) (Yu *et al*. 2011). The great advantage of image-based modeling is that it facilitates the numerical analysis of inhomogeneous materials. Because the FEM and FDTD are more advantageous when analyzing inhomogeneous regions compared to BEM, image-based modeling has been increasingly incorporated into the FEM and FDTD approaches. However, the FEM cannot deal with infinite and semi-infinite domains. To overcome this disadvantage, absorbing boundaries, such as PML (Givoli 2004), etc., have been applied to the FEM framework. There are no missing boundaries that can accurately satisfy the radiation condition of scattered waves in infinite space.

Therefore, in this study, a coupling method was developed for the regions containing both finite inhomogeneous and infinite characteristics. The CQBEM and FEM are utilized for treating the infinite homogeneous and finite inhomogeneous regions, respectively, to maximize the advantages of each method. The proposed coupling method has already been developed for 2-D anti-plane wave propagation by our research group (Saitoh *et al*. 2016). Consequently, in this study, the previously proposed method for 2-D anti-plane wave propagation is extended to include 2-D elastic wave propagation, which requires a more difficult formulation (Eringen and Suhubi 1975).

In the following section, the problem at hand is introduced. 2-D elastic wave propagation in an infinite space with a finite region is considered. Next, the CQM and CQBEM formulations are discussed. Then, a brief description of the image-based modeling and FEM formulations for 2-D elastodynamics are introduced. The analysis of elastic wave scattering by an inclusion is implemented using the proposed method to confirm its computational accuracy. Finally, elastic wave scattering by an inhomogeneous solid in an infinite space is demonstrated to validate the proposed coupling method.

2. Problem

The small index used throughout this study, such as $(\,)_i$, ranges from 1 to 2, unless stated otherwise. Additionally, summation over repeated subscripts is implied throughout this paper.

Let us consider elastic wave propagation, scattering and transmission in an infinite space Ω_B over a finite region Ω_F and boundary Γ, as depicted in Fig. 1. The infinite space Ω_B and finite region Ω_F are treated by the CQBEM and FEM, respectively. Displacement $u_i(\boldsymbol{x},t)$ at position $\boldsymbol{x}$ and time t in both isotropic domains Ω_B and Ω_F satisfy the Navier-Cauchy equation in the time-domain, which is stated as follows:

$$\rho\ddot{u}_i(\boldsymbol{x},t) = \mu u_{i,jj}(\boldsymbol{x},t) + (\lambda+\mu)u_{j,ij}(\boldsymbol{x},t) \tag{1}$$

$$u_i(\boldsymbol{x},0) = 0, \qquad \dot{u}(\boldsymbol{x},0) = 0 \tag{2}$$

where Eq. (2) demonstrates the initial condition. In addition, λ and μ are the Lamé constants and ρ is the density. The dot $(\dot{\,})$ and the the symbol $(\,)_{,i}$ represent the partial derivative with

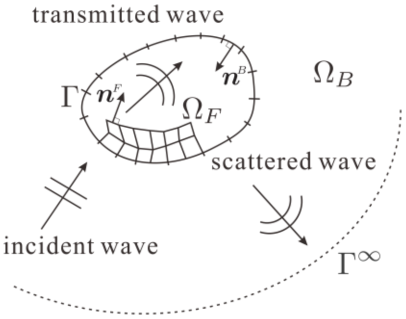

Fig. 1 2-D elastic wave scattering in an infinite and heterogeneous area

respect to the time t $(\partial/\partial t)$ and space x_i $(\partial/\partial x_i)$, respectively. In Eq. (1), the body force term is neglected. In Fig. 1, $\boldsymbol{n}^B$ and $\boldsymbol{n}^F$ are the unit normal vectors at a point $\boldsymbol{x}$ with respect to the outer domain Ω_B and inside domain Ω_F, respectively. Displacement $u_i(\boldsymbol{x},t)$ satisfies Eq. (1) in each domain Ω_B and Ω_F and is calculated using the method that couples the CQBEM and FEM presented in this study.

3. CQBEM formulation

3.1 Time domain boundary integral equation

For an infinite homogeneous region Ω_B containing inhomogeneous infinite region Ω_F, CQBEM is utilized to treat the radiation condition on the infinite boundary Γ^∞, as depicted in Fig. 1. The time domain boundary integral equation for domain Ω_B can be expressed as follows:

$$C_{ij}(\boldsymbol{x})u_j(\boldsymbol{x},t) = u_i^{\text{in}}(\boldsymbol{x},t) + \int_\Gamma U_{ij}(\boldsymbol{x},\boldsymbol{y},t) * q_j(\boldsymbol{y},t)d\Gamma_y - \int_\Gamma S_{ij}(\boldsymbol{x},\boldsymbol{y},t) * u_j(\boldsymbol{y},t)d\Gamma_y \tag{3}$$

where $C_{ij}(\boldsymbol{x})$ is the free term and $U_{ij}(\boldsymbol{x},\boldsymbol{y},t)$ and $S_{ij}(\boldsymbol{x},\boldsymbol{y},t)$ are the time-domain fundamental solution and corresponding traction fundamental solution for 2-D elastodynamics, respectively. The symbol $*$ represents the convolution integral with respect to time t and $q_j(\boldsymbol{y},t)$ denotes the traction component. In addition, $u_i^{\text{in}}(\boldsymbol{x},t)$ denotes an incident wave.

In general, the calculation of the time-domain boundary integral equation defined in Eq. (3) is unstable when the time increment Δt is small. However, image-based FEM (IMFEM) requires a small time increment to guarantee the accuracy of time-domain solutions. Therefore, in this study, the convolution integral of the time-domain boundary integral Eq. (3) is numerically approximated using the CQM proposed by Lubich (1998) to obtain stable numerical solutions in the time-domain.

3.2 Convolution quadrature method (CQM)

Before applying the CQM to the time-domain boundary integral equation (3), we briefly discuss the CQM proposed by Lubich (1998).

In general, the convolution integral is expressed as follows:

$$f * g(t) = \int_0^t f(t-\tau)g(\tau)d\tau \tag{4}$$

The convolution integral defined in Eq. (4) can be numerically approximated using CQM as follows:

$$f * g(n\Delta t) = \sum_{k=0}^{n} \omega_{n-k}(\Delta t)g(k\Delta t), \quad (n = 0,1,\cdots,N) \tag{5}$$

where time t is divided into N equal time steps $(t = n\Delta t, n = 0,\dots,N)$ with a time increment of Δt. The function ω_n is the weight function, which is defined as follows:

$$\omega_n(\Delta t) \simeq \frac{\mathcal{R}^{-n}}{L}\sum_{l=0}^{L-1}\hat{f}\left(\frac{\gamma(z_l)}{\Delta t}\right)e^{-\frac{2\pi i n l}{L}} \tag{6}$$

where $\hat{f}$ denotes the Laplace transformation of the original kernel function $f(t)$ defined in Eq. (4). Additionally, i is the imaginary unit and $z_l = \mathcal{R}\mathrm{e}^{2\pi \mathrm{i} l/L}$. $\mathcal{R}$ and L are CQM parameters. Parameter $\mathcal{R}$ can be determined using the target accuracy ϵ when constructing Eq. (5), which is defined as follows:

$$\mathcal{R}^L = \sqrt{\epsilon} \tag{7}$$

Moreover, in Eq. (6), function $\gamma(z)$ is given as follows:

$$\gamma(z) = \sum_{k=1}^{n}\frac{1}{k!}(1-z)^k \tag{8}$$

In Eq. (8), $n = 1$ or $n = 2$, which are denoted as BDF1 and BDF2 (Schanz 2001), respectively, must be considered. Applying Eq. (5) to the convolutions of the time-domain boundary integral equation defined in Eq. (3) and using the weight function $\omega_n(\Delta t)$ defined in Eq. (6), we can solve the time-domain boundary integral equation (3) without using the time-domain fundamental solution, which is necessary for classical time-domain BEM tasks (Niwa *et al.* 1980). Therefore, the CQBEM is very useful for problems in which no time-domain fundamental solutions are known, such as viscoelastodynamic (Saitoh and Takeda 2021) and poroelastodynamic problems (Saitoh *et al.* 2014). For such problems, the corresponding Laplace-domain fundamental solutions are well known. Consequently, the use of the CQBEM can expand the application spectrum of time-domain BEMs. Some engineering problems have been solved using the CQBEM, which overcomes the disadvantages of the classical time-domain BEM applications (Xinzhong and Shunming 2018).

3.3 Discretization for time and space

As mentioned in the previous section, time discretization is carried out using CQM. On the other hand, the spatial discretization is performed using the linear interpolation function. Considering the interpolation function $\phi^p(\xi)$ for a local coordinate ξ on the discretized boundary Γ_j $(j = 1,\dots,M_B)$, the displacement u_i and traction q_i are approximated on the boundary Γ_j as follows:

$$u_i = \sum_{p=1}^{2} \phi^p(\xi) u_i^p, \quad q_i = \sum_{p=1}^{2} \phi^p(\xi) q_i^p \tag{9}$$

where u_i^p and q_i^p are the displacement and traction components, respectively, at node p of a discretized boundary element Γ_j obtained by spatial discretization. Applying the CQM presented in Eq. (5) and linear interpolations stated in Eq. (9) to the time-domain boundary integral equation (3) for time and space discretization, respectively, and taking the limit $\boldsymbol{x} \in \Gamma$, the discretized boundary integral equation can be obtained as follows:

$$\frac{1}{2}u_i(\boldsymbol{x}, n\Delta t) = u_i^{\text{in}}(\boldsymbol{x}, n\Delta t) + \sum_{\alpha=1}^{M_B}\sum_{k=1}^{n}\left[A_{ij}^{n-k,\alpha}(\boldsymbol{x}) q_j(\boldsymbol{y}^\alpha, k\Delta t) - B_{ij}^{n-k,\alpha}(\boldsymbol{x}) u_j(\boldsymbol{y}^\alpha, k\Delta t)\right] \tag{10}$$

where A_{ij}^m and B_{ij}^m are the influence functions, which are obtained using Eqs. (5) and (6) as follows:

$$A_{ij}^{m,\alpha}(\boldsymbol{x}) = \frac{\mathcal{R}^{-m}}{L}\sum_{l=0}^{L-1}\sum_{p=1}^{2}\left[\int_\Gamma \hat{U}_{ij}(\boldsymbol{x}, \boldsymbol{y}^\alpha, s_l)\phi^p\right] e^{-\frac{2\pi i m l}{L}} d\Gamma_y \tag{11}$$

$$B_{ij}^{m,\alpha}(\boldsymbol{x}) = \frac{\mathcal{R}^{-m}}{L}\sum_{l=0}^{L-1}\sum_{p=1}^{2}\left[\int_\Gamma \hat{S}_{ij}(\boldsymbol{x}, \boldsymbol{y}^\alpha, s_l)\phi^p\right] e^{-\frac{2\pi i m l}{L}} d\Gamma_y \tag{12}$$

where s_l is the Laplace parameter. Eqs. (11) and (12) are represented in the form of Fourier transforms. Therefore, Eqs. (11) and (12) can be efficiently calculated using the fast Fourier transform (FFT) if the CQM parameter L is set to $L = N$, where N is the total number of time steps. Kernels $\hat{U}_{ij}(\boldsymbol{x}, \boldsymbol{y}, s)$ and $\hat{S}_{ij}(\boldsymbol{x}, \boldsymbol{y}, s)$ are the Laplace-domain fundamental solutions and double-layer kernel for 2-D elastodynamics, respectively, which are given by

$$\hat{U}_{ij}(\boldsymbol{x}, \boldsymbol{y}, s) = \frac{1}{\mu}\left[g_T\delta_{ij} - \frac{1}{s_T^2}(g_T - g_L)_{,ij}\right] \tag{13}$$

$$\hat{S}_{ij}(\boldsymbol{x}, \boldsymbol{y}, s) = -\delta_{ij} n_k^y (g_T)_{,k} - n_i^y (g_T)_{,j} - \left(1 - 2\frac{c_T^2}{c_L^2}\right) n_j^y (g_L)_{,i} + \frac{2}{s_T^2} n_k^y (g_T - g_L)_{,ijk} \tag{14}$$

In Eq. (14), c_L and c_T denote the wave velocities of P- and S-waves, respectively. δ_{ij} and n_k^y denote the Kronecker delta and unit outer normal vector of the boundary element with $\boldsymbol{y}$, respectively. In addition, g_L and g_T are defined as

$$g_L(r) = \frac{1}{2\pi}K_0(s_L r), \qquad g_T(r) = \frac{1}{2\pi}K_0(s_T r) \tag{15}$$

where r is defined as $r = |\boldsymbol{x} - \boldsymbol{y}|$ and K_0 is the second kind of modified Bessel function of the 0-th order. Parameter s_β is given by $s_\beta = s_l/c_\beta\ (\beta = L \text{ or } T)$. In the discretized boundary integral Eq. (10) at the n-th time step, Eq. (10) can be rewritten in the matrix form as follows:

$$[\boldsymbol{B}^0]\{\boldsymbol{u}\}^n - [\boldsymbol{A}^0]\{\boldsymbol{q}\}^n = \{\boldsymbol{u}^{\text{in}}\}^n + \sum_{k=1}^{n-1}\left[[\boldsymbol{A}^{n-k}]\{\boldsymbol{q}\}^k - [\boldsymbol{B}^{n-k}]\{\boldsymbol{u}\}^k\right] \tag{16}$$

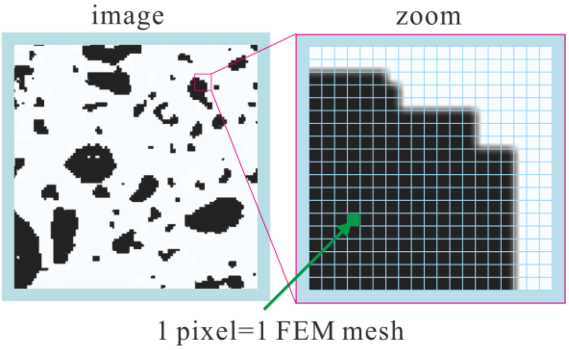

Fig. 2 A digital image data and magnified local area

where $[\boldsymbol{A}^m]$ and $[\boldsymbol{B}^m]$ are the assembling matrices defined in Eqs. (11) and (12), respectively. $\{\boldsymbol{u}^{\text{in}}\}^n$ denotes the incident wave vector at the n-th time step. In addition, $\{\boldsymbol{u}\}^n$ and $\{\boldsymbol{q}\}^n$ are the displacement and traction vectors at the n-th time step, respectively. In Eq. (16), $\{\boldsymbol{u}\}^k$ and $\{\boldsymbol{q}\}^k$ on the right-hand side are known at the n-th time step. Therefore, Eq. (16) can be solved starting from the first time step $n = 1$ with the initial conditions to the last time step $n = N$.

4. Image-based FEM (IMFEM) formulation

Next, a formulation of the time domain IMFEM is presented. In this section, first, the image-based modeling is briefly described. Subsequently, the time-domain FEM formulation using image-based modeling is explained. As mentioned previously, FEM is the de facto standard method in the computational engineering field as shown in literatures, e.g., (Logan 2016).

4.1 Image-based modeling

Image-based modeling is a method for modeling the shape data of an object using a digital image. Generally, digital images are represented by a set of pixels, as depicted in Fig. 2. In image-based modeling, one pixel in an image is considered a finite element, as depicted in Fig. 2. Therefore, a finite element is square in 2-D problems. The depth direction can be considered by taking many tomographic images for 3-D problems. Subsequently, a finite element is defined as a cubic shape in 3-D problems. In general, it is difficult to represent curves (or curved surfaces) of analysis objects smoothly in image-based modeling, shown in Fig. 2, because curves need to be approximated by members of squares in 2-D problems. However, in FEM modeling, complex analysis targets or problems can be easily addressed if corresponding images can be prepared. Therefore, for such complex problems, the required preprocessing time can be reduced if image-based modeling is used.

4.2 Finite element equation based on the image-based modeling

In general, FEM formulation can be found in many textbooks, for example, (Logan 2016). Therefore, the formulation of a finite element method based on image-based modeling is briefly described in this section. The Galerkin method is applied to the spatial discretization described in Eq. (1). By multiplying Eq. (1) by a weight function, $N_i (i = 1, \dots, 4)$ (Hughes 1987), and integrating the resulting equation over the analysis domain $\Omega_F \simeq \sum_{e=1}^{M_F} v_e$, we can obtain the following equation:

$$\sum_{e=1}^{M_F} \int_{v_e} N_\alpha \left(\mu u_{i,jj} + (\lambda + \mu) u_{j,ij} - \rho \ddot{u}_i \right) dv_e = 0 \tag{17}$$

where M_F denotes the number of finite elements and v_e is the e-th finite element region. The following equation can be obtained using the Gauss-Green theorem:

$$\int_{v_e} N_\alpha u_{i,jj} dv_e = \int_{s_e} N_\alpha u_{i,j} n_j ds_e - \int_{v_e} N_{\alpha,j} u_{i,j} dv_e \tag{18}$$

where s_e represents a boundary of the finite element v_e. Substituting Eq. (18) into Eq. (17), assuming that the Lamé constants λ and μ are used and the density ρ takes constant values for each finite element, Eq. (17) can be rewritten as follows:

$$\begin{aligned} &\sum_{e=1}^{M_F} \mu \left\{ \int_{s_e} N_\alpha u_{i,j} n_j ds_e - \int_{v_e} N_{\alpha,j} u_{i,j} dv_e \right\} + \sum_{e=1}^{M_F} \lambda \left\{ \int_{s_e} N_\alpha u_{j,j} n_\alpha ds_e - \int_{v_e} N_{\alpha,i} u_{j,j} dv_e \right\} \\ &\quad + \sum_{e=1}^{M_F} \mu \left\{ \int_{s_e} N_\alpha u_{j,i} n_j ds_e - \int_{v_e} N_{\alpha,j} u_{j,i} dv_e \right\} - \sum_{e=1}^{M_F} \rho \int_{v_e} N_\alpha \ddot{u}_i dv_e = 0 \end{aligned} \tag{19}$$

Eq. (19) can be rewritten with respect to an integration over the finite element v_e and its boundary s_e as follows:

$$\begin{aligned} &\sum_{e=1}^{M_F} \sum_{\beta=1}^{4} \left[\mu \int_{v^e} N_{\alpha,j} N_{\beta,j} dv_e \cdot u_{i\beta}^e + \lambda \int_{v^e} N_{\alpha,i} N_{\beta,j} dv_e \cdot u_{j\beta}^e + \mu \int_{v^e} N_{\alpha,j} N_{\beta,i} dv_e \cdot u_{j\beta}^e \right] \\ &\quad + \sum_{e=1}^{M_F} \sum_{\beta=1}^{4} \left[\rho \int_{v^e} N_\alpha N_\beta dv_e \cdot \ddot{u}_{i\beta}^e \right] - \sum_{e=1}^{M_F} \sum_{\beta=1}^{4} \left[\int_{s^e} N_\alpha q_{i\beta} ds_e \right] = 0 \end{aligned} \tag{20}$$

where $u_{i\beta}^e$ and $q_{i\beta}^e$ are the displacement and traction components, respectively, at node β of a rectangular finite element v_e. The second term in Eq. (20) contains a partial derivative with respect to time t. Therefore, applying the backward differential approximations,

$$\dot{u}_i^n = \frac{u_i^n - u_i^{n-1}}{\Delta t}, \ddot{u}_i^n = \frac{u_i^n - 2u_i^{n-1} + u_i^{n-2}}{\Delta t^2} \tag{21}$$

to Eq. (20) and moving the terms with respect to the displacement $u_{i\beta}^n$ at the n-th time step to the left-hand side, while moving the remaining terms with respect to $u_{i\beta}^{n-1}$ and $u_{i\beta}^{n-2}$ to the right-hand side, we arrive at the following matrix form:

$$\Delta t^2 \{[\boldsymbol{K}] + [\boldsymbol{M}]\} \{\boldsymbol{u}\}^n - \Delta t^2 [\boldsymbol{Q}] \{\boldsymbol{q}\}^n = 2[\boldsymbol{M}] \{\boldsymbol{u}\}^{n-1} - [\boldsymbol{M}] \{\boldsymbol{u}\}^{n-2} \tag{22}$$

where $\{\boldsymbol{u}\}^n$ and $\{\boldsymbol{q}\}^n$ are the displacement and traction vectors at the n-th time step, respectively. Matrix $[\boldsymbol{M}]$ is the global mass matrix and can be obtained using the second term on

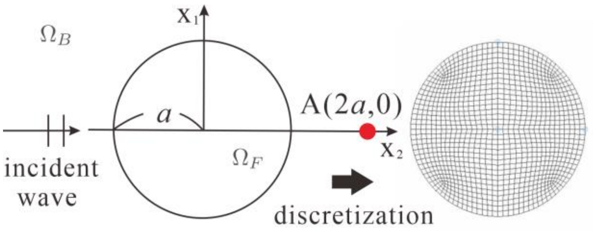

Fig. 3 Analysis model for accuracy verification and its CQBEM-FEM mesh

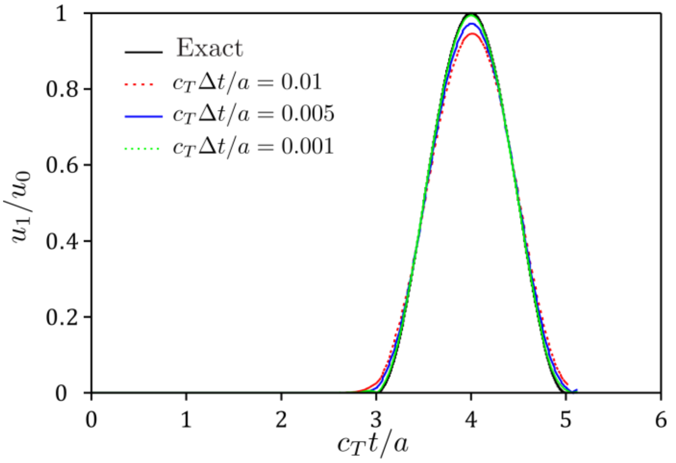

Fig. 4 Time variation of total displacements at point A depicted in Fig. 3 for various time increments Δt

the left-hand side belonging Eq. (20). Matrix $[\boldsymbol{K}]$ is the global stiffness matrix calculated by the first term on the left-hand side belonging to Eq. (20). Matrix $[\boldsymbol{Q}\}$ can be obtained from the third term on the left-hand side belonging to Eq. (20). Eq. (22) can be solved at the n-th time step using the solutions obtained at the previous $n-1$ and $n-2$-th time steps. The procedure for obtaining the final form of Eq. (22) is the same as that followed for 2-D SH wave propagation (Saitoh *et al*. 2016). Thus, Eq. (22) can be solved step by step starting from the initial and boundary conditions of the problem to be solved.

5. Coupling of CQBEM and image-based FEM

A brief description of the coupling between the CQBEM and image-based FEM frameworks is presented in this section. In general, the equivalent boundary element coupling and finite element coupling methods are known in the field of the classical coupling method for BEM and FEM frameworks (Fukui 1987, Von 1990, Aour 2006). In this study, the equivalent boundary element coupling method was considered for coupling the CQBEM and image-based FEM frameworks. In the equivalent boundary element coupling algorithm, the finite element domain Ω_F is considered as an equivalent boundary element. The existing BEM formulation can be easily applied to this algorithm.

To solve Eqs. (16) and (22) simultaneously, the time increment Δt for the CQBEM framework is set to be the same as that for the image-based FEM framework. The following continuity

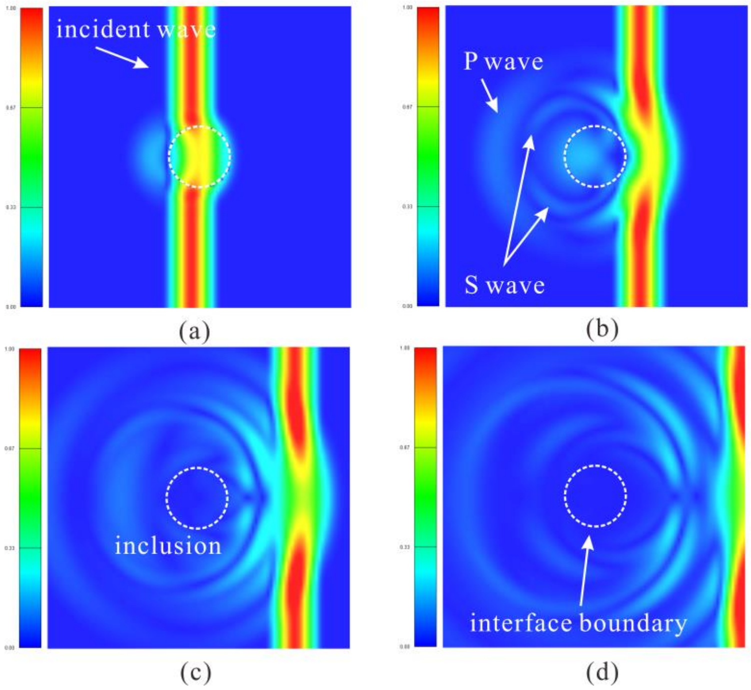

Fig. 5 Elastic wave scattering caused by a circular inclusion at (a)$n = 100$, (b)$n = 200$, (c)$n = 300$, and (d)$n = 400$ time steps

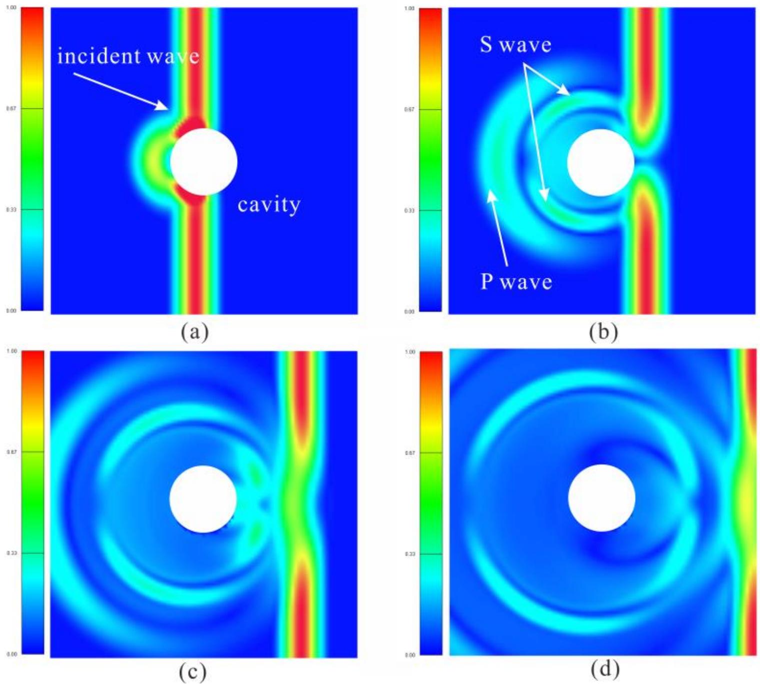

Fig. 6 Elastic wave scattering caused by a cavity at (a)$n = 100$, (b)$n = 200$, (c)$n = 300$, and (d)$n = 400$ time steps

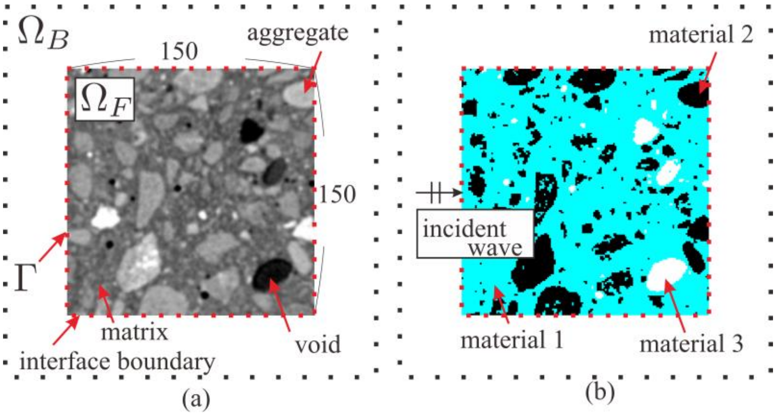

Fig. 7 Image-based modeling obtained by using an X-ray CT image (a) original X-ray CT image and (b) processed image data

boundary conditions between the boundary element region Ω_B and finite element region Ω_F are considered:

$$u_{iF}(\boldsymbol{x},t)=u_{iB}(\boldsymbol{x},t),\quad q_{iF}(\boldsymbol{x},t)+q_{iB}(\boldsymbol{x},t)=0 \tag{23}$$

where the subscripts B and F denote the displacement and traction components in the boundary element region Ω_B and finite element region Ω_F, respectively. By applying the boundary conditions depicted in Eq. (23) to both Eqs. (16) and (22), and solving the resulting matrix through time steps, the unknown displacements and tractions at the boundary Γ and in the finite domain Ω_F at all time steps can be obtained. Once the unknown displacements and tractions on the boundary Γ are obtained, the displacement u_i in the outer space Ω_B can be calculated using Eq. (3) with the free term $C_{ij}=1$ for $i=j$, and otherwise $C_{ij}=0$ for $i\neq j$.

6. Numerical examples

Some numerical examples are presented in this section. The accuracy parameter ϵ defined in Eq. (7) is set to $\epsilon=1.0\times10^{-12}$ for all the following calculations. The time increment Δt used for the CQBEM frameworks is the same as that used for the image-based FEM framework. In the numerical examples, the incident plane P-wave propagating in the x_1 direction is considered for the 2-D infinite domain Ω_B as follows:

$$\begin{aligned} u_i^{\text{in}}(\boldsymbol{x},t) &= u_0\frac{1}{2}\delta_{i1}(1-\cos\,2\pi\alpha), \\ \alpha &= \begin{cases} \dfrac{c_L}{\lambda_L}\left(t-\dfrac{x_1+a'}{c_L}\right) & \text{for}\quad (0\le\alpha\le1) \\ 0 & \text{for}\quad \text{otherwise} \end{cases} \end{aligned} \tag{24}$$

6.1 Accuracy confirmation

Before presenting the numerical results obtained by the proposed method, the coupling of the CQBEM and classical FEM without image-based modeling was validated and confirmed.

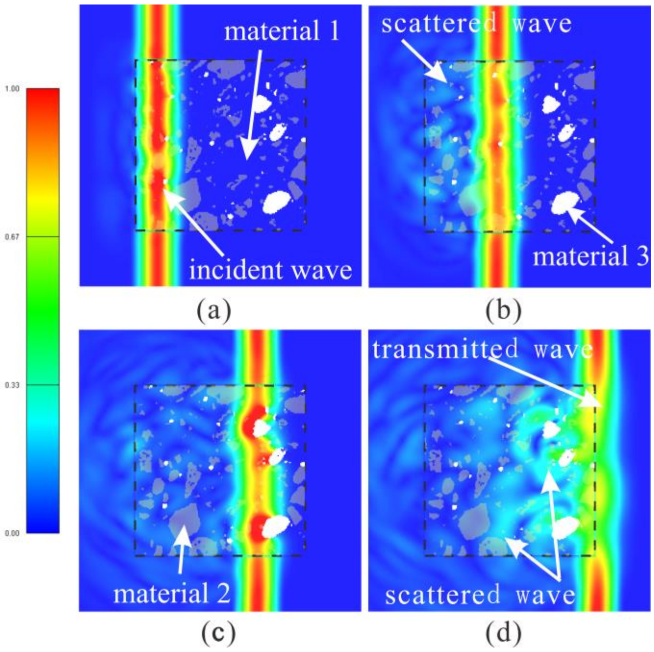

Fig. 8 Total wave fields $|\boldsymbol{u}|/u_0$ around the inhomogeneous area at (a)$n=100$, (b)$n=200$, (c)$n=300$, and (d)$n=400$ time steps

The scattering of an incident plane P-wave by a circular object, shown in Fig. 3, was solved by the coupling method without image-based modeling to verify the individual computational accuracy of CQBEM and FEM. In this problem, if the material parameters of an object Ω_F are the same as those of an infinite elastic solid Ω_B, and the continuous boundary conditions for the displacement u_i and traction q_i on the boundary Γ are imposed as depicted in Eq. (23), the solutions of the boundary value problems are equivalent to those for an incident wave $u_i^{\mathrm{in}}(\boldsymbol{x},t)$.

Fig. 4 presents the time histories of the horizontal displacement u_1 at the point A depicted in Fig. 3, which are obtained by using several time increments Δt. Parameter a, which denotes the radius of the object Ω_F presented in Fig. 3, is used as $a'=1.0$ in Eq. (24). The exact solutions, namely, the incident waves $u_i^{\mathrm{in}}(\boldsymbol{x},t)$ for this problem, are also indicated by the solid line to evaluate the accuracy in Fig. 4. The incident wavelength λ_L, density ρ, and P-wave velocity c_L values are given as $\lambda_L=2.0$, $\rho=1.0$, and $c_L=1.0$, respectively. In this case, Poisson's ratio ν in domain Ω_B is given as $\nu=0.25$. Object Ω_F is discretized into $(M_F=)1092$ rectangular finite elements, as shown on the right side in Fig. 3. The number of boundary elements is $M_B=104$ in this case. There are 1145 node points in total.

It can be observed that the peak values of the horizontal displacement u_1 at point A depicted in Fig. 3 are not accurate compared to the exact solutions when the time increments are $\Delta t=0.01$ and $\Delta t=0.005$. However, the results obtained by coupling CQBEM and FEM with time step of $\Delta t=0.001$ were in good agreement with the exact solutions, which is demonstrated in Fig. 4. A small time-step size, $\Delta t=0.001$, yields more accurate results than those obtained with $\Delta t=0.01$ and $\Delta t=0.005$. This numerical computation was executed in a stable manner, even for small time increments $\Delta t=0.001$ owing to using CQBEM.

6.2 Elastic wave scattering caused by a circular inclusion

Next, an elastic wave scattering caused by a circular inclusion was solved using the coupled method. For this calculation, the geometric model shown in Fig. 3 in the previous section 6.1 is used. However, different parameters are considered for Ω_F which is introduced as an inclusion here. The wavelength λ_L is set as $\lambda_L = 2.0$. The ratio between the P- and S-wave velocities, c_{LB} and c_{TB}, respectively, in the domain Ω_B is given as $c_{LB}/C_{TB} = \sqrt{2}$. In addition, the ratio between the P- and S-wave velocities, c_{LF} and c_{TF}, respectively, in the domain Ω_F is $c_{LF}/c_{TF} = \sqrt{2}$. The inclusion with radius $a = 1$ is discretized according to the number of finite elements $M_F = 22500$. Accordingly, the number of boundary elements M_B is set as $M_B = 600$. Enough nodes per wavelength are considered. In addition, the time increment $\Delta t \simeq 0.02$ and total time steps $N = 1024$.

Figs. 5 (a)-(d) depict the total displacements $|\boldsymbol{u}|$ around the inclusion at $n = 100$, $n = 200$, $n = 300$, and $n = 400$ time steps, subjected to the incident P-wave defined in Eq. (24). For comparison, the results regarding the case in which the infinite domain Ω_F is a cavity with a traction-free boundary condition is presented in Fig. 6. In Figs. 5 (a)-(d), the dashed white circles indicate the boundary between the domains Ω_B and Ω_F. In addition, the white circles indicate the cavity in Fig. 6.

In Fig. 5(a), the scattered P-wave can be seen in front of the inclusion. The incident P-wave inside the inclusion travels faster than that in the infinite outer domain Ω_B because the P-wave velocity c_{LF} in the inclusion Ω_F is larger than c_{LB} in the domain Ω_B. However, if the object Ω_F is a cavity, the incident P-wave is totally scattered by the cavity as shown in Fig. 6. Moreover, a scattered S-wave can be generated by the mode conversion of the incident P-wave as shown in Fig. 5(b). Part of the P-wave is scattered, while the rest is transmitted, as shown in Figs. 5(c) and (d). From these numerical results, it can be observed that the CQBEM is properly coupled with image-based FEM.

6.3 Elastic wave scattering by many inclusions

As a final numerical example, elastic wave scattering by many inclusions was analyzed using the proposed method. The inclusions were modeled using image-based modeling in this analysis.

6.3.1 Preparation of analysis model using image-based modeling

Fig. 7(a) depicts the image used in this analysis, which is taken by an X-ray CT for a concrete block with many aggregates. The number of pixels of the image is $150 \times 150 = 22500$. Therefore, the total number of finite and boundary elements M_F and M_B are $M_F = 22500$ and $M_B = 600$, respectively, if one pixel matches one finite element.

To create the analysis model, first, each pixel of a grayscale digital image is represented by an integer from 0 to 255, which is depicted in Fig. 7(a). Three thresholds were set (from 0 to 255) to divide the infinite region Ω_F into three materials. In this analysis, which is presented in Fig. 7(b), the three infinite domains are distinguished from each other using the grayscale values from 151 to 255 as material 1, those from 61 to 150 as the material 2, and those from 0 to 60 as the material 3. As shown in Fig. 7, the finite element modeling for inhomogeneous regions can be easily implemented using the image-based modeling for a digital image as an analysis object.

6.3.2 Results obtained by proposed method

As mentioned in section 6.3.1, a scattering problem in an infinite domain Ω_B including a finite inhomogeneous region Ω_F is considered here. In this analysis, the material parameters of the infinite domain Ω_B were set to be the same as those of material 1 located in the inhomogeneous region Ω_F. The incident P-wave, defined in Eq. (24) with $a' = 3a$, was also considered. Here, the parameters, namely, the incident wavelength λ_L and P-wave velocity c_L in each of the three materials are defined as $\lambda_{L\gamma}$ and $c_{L\gamma}$, respectively, using the subscripts $\gamma(\gamma = 1,2,3)$, which indicate the material number set by the image-based modeling depicted in Fig. 7. The wavelength λ_{L1} of the incident P-wave was set as $\lambda_{L1} \simeq 0.66$. The ratios between the P- and S-wave velocities in material 1, 2, and 3 were $c_{L1}/c_{T1} = 1.78$, $c_{L2}/c_{T2} = 1.76$, and $c_{L3}/c_{T3} = 1.73$, respectively. Accordingly, the Poisson's ratio values ν_γ for materials 1, 2, and 3 are given as ν_1=0.27, $\nu_2 = 0.26$, and $\nu_3 = 0.25$, respectively. In Fig. 7, the dashed rectangles indicate the interface boundary Γ. On the other hand, the outer dashed black rectangles indicate the infinite boundary. However, the outer dashed rectangles do not need to be considered because CQBEM can deal with the infinite boundaries without any modification.

Figs. 8(a), (b), (c), and (d) depict the total wave fields $|\boldsymbol{u}|/u_0$ around the inhomogeneous area at (a) $n = 100$, (b) $n = 200$, (c) $n = 300$, and (d) $n = 400$ time steps, respectively. The incident P-wave enters the inhomogeneous domain Ω_F, as shown in Fig. 8(a). Material 2 is smaller than the wavelength λ_{LB} of the incident P-wave. In addition, material 2 is modeled as an inclusion. Therefore, the incident P-wave can propagate inside inclusions in the domain Ω_F, as depicted in Fig. 8(b), by repeating the multiple scattering. Accordingly, no scattered waves with large amplitudes can be seen in Figs. 8(a) and (b). However, scattered waves with large amplitudes are observed, which are presented in Figs. 8(c) and (d), because the acoustic impedance between the matrix and material 3 is large. In addition, scattered waves generated by the interaction between the incident P-wave and materials 2 and 3 propagate to infinity, and no scattered waves from the infinite boundaries can be observed owing to using the CQBEM framework over domain Ω_B. In addition, no useless scattered waves can be observed at the interface boundary between Ω_B and Ω_F. Therefore, we can conclude that the CQBEM and image-based FEM frameworks are combined without any problems for 2-D elastodynamic problems.

7. Conclusions

In this study, a method for coupling the CQBEM and image-based FEM frameworks was developed for 2-D elastodynamic problems. The proposed coupling method has the advantages of both the CQBEM and image-based FEM. The proposed method can easily deal with infinite regions without difficulties using CQBEM and inhomogeneous regions using image-based FEM. Some elastic wave scattering problems were solved to validate the proposed method. In the future, the proposed coupling method for 2-D elastodynamic problems will be extended to 3-D problems. In addition, the fast multipole method (FMM) (Greengard and Rokhlin 1987, Rokhlin 1985) and adaptive cross approximation method (Bebendorf (2008)) will be applied to accelerate calculating a part of the matrix-vector products of the CQBEM. The proposed method will be applied to the simulation of ultrasonic waves in nondestructive testing fields (Rose 1999).

Acknowledgment

This study was supported by JSPS KAKENHI (21K0423100, 24K00966), Joint Usage/Research Center for Interdisciplinary Large-scale Information Infrastructures, and High-Performance Computing Infrastructure in Japan (Project IDs: jh230036, jh240035). Support was also provided by the SECOM Science and Technology Foundation.

References

Abreu, A.I., Carrer, J.A.M. and Mansur, W.J. (2003), “Scalar wave propagation in 2D: A BEM formulation based on the operational quadrature method”, *Eng. Anal. Bound. Elem.*, **27**, 101-105. https://doi.org/10.1016/S0955-7997(02)00087-5

Aour, B., Rahmani, O. and Nait-Abdelaziz, M. (2006), “A coupled FEM/BEM approach and its accuracy for solving crack problems in fracture mechanics”, *Int. J. Solids Struct.*, **44**, 2523-2539.

Azqandi, M.S., Hassanzadeh, M. and Arjmand, M. (2019), “Sensitivity analysis based on complex variables in FEM for linear structures”, *Adv. Comput. Des.*, **4**(1), 15-32. https://doi.org/10.12989/acd.2019.4.1.015

Bebendorf, M. (2008), *Hierarchical Matrices: A Means to Efficiently Solve Elliptic Boundary Value Problems*, Springer-Verlag.

Beskos, D. (1987), *Boundary Element Methods in Mechanics*, North Holland.

Chung, S.Y., Han, T.S. and Kim S.Y. (2015) “Reconstruction and evaluation of the air permeability of a cement paste specimen with a void distribution gradient using CT images and numerical methods”, *Constr. Build. Mater.*, **87**(15), 45-53. https://doi.org/10.1016/j.conbuildmat.2015.03.103

Eringen, A.C. and Suhubi, E.S. (1975), *Elastodynamics: Vol.1 and 2*, Academic Press Inc.

Fellinger, P., Marklein, R., Langenberg, K. J. and Klaholz, S. (1995), “Numerical modeling of elastic wave propagation and scattering with EFIT -elastodynamic finite integration technique”, *Wave Motion*, **21**(1), 47-66. https://doi.org/10.1016/0165-2125(94)00040-C

Fukui. T, and Ishida, Y. (1987), “Time marching BE-FE method in wave problem”, *Proceedings of the 1st Japan-China Symposium Boundary Element Methods*, 95-106.

Givoli, D. (2004), “High-order local non-reflecting boundary conditions: a review”, *Wave Motion*, **39**, 319-326. https://doi.org/10.1016/j.wavemoti.2003.12.004

Greengard, L. and Rokhlin, V. (1987), “A fast algorithm for particle simulations”, *J. Comput. Phys.*, **73**, 325-348.

Hughes, T.J.R. (1987), *The Finite Element Method: Linear Static and Dynamic Finite Element Analysis*, Dover Publications, New York, N.Y., U.S.A.

Logan, D.L. (2016), *A First Course in the Finite Element Method: SI Edition*, Cl-Engineering.

Lubich, C. (1998), “Convolution quadrature and discretized operational calculus I”, *Numerische Mathematik*, **52**, 129-145. https://doi.org/10.1007/BF01398686

Lubich, C. (1998), “Convolution quadrature and discretized operational calculus II”, *Numerische Mathematik*, **52**, 413-425. https://doi.org/10.1007/BF01462237

Mansur, W.J. and Brebbia, C.A. (1983), “Transient elastodynamics using a time-stepping technique”, *Bound. Elem.*, 677-698.

Nakahata, K, Hirose, S., Schbert, F. and Kohler, B. (2009), “Image based EFIT simulation for nondestructive ultrasonic testing of austenitic steel”, *J. Solid Mech. Mater. Eng.*, **3**(12), 1256-1262. https://doi.org/10.1299/jmmp.3.1256

Niwa, Y., Fukui, T., Kato, S. and Fujiki, K. (1980), “An application of the integral equation method to two-dimensional elastodynamics”, *Theor. Appl. Mech.*, **28**, 281-290.

Rokhlin, V. (1985), “Rapid solution of integral equations of classical potential theory”, *J. Comput. Phys.*, **60**, 187-207.

Rose J.L. (1999), *Ultrasonic Waves in Solid Media*, Cambridge University Press, Cambridge, Cambridgeshire, U.K.

Saitoh, T. (2024), "Convolution quadrature time-domain boundary element method for antiplane anisotropic viscoelastic wave propagation", *Eng. Anal. Bound. Elem.*, **164**, 105753. https://doi.org/10.1016/j.enganabound.2024.105753

Saitoh, T., Chikazawa, F. and Hirose, S. (2014), "Convolution quadrature time-domain boundary element method for 2-D fluid-saturated porous media", *Appl. Math. Modell.*, **38**, 3724-3740. https://doi.org/10.1016/j.apm.2014.02.009

Saitoh, T., Ichikawa, R. and Inagaki, Y. (2016), "Development of coupling method of convolution quadrature BEM and image-based FEM for 2-D wave propagation in time-domain", *J. Japan Soc. Comput. Meth. Eng.*, **16**, 1-6 (in Japanese).

Saitoh, T. and Takeda, H. (2021), "Convolution quadrature time-domain boundary element method for viscoelastic wave scattering by many cavities in 3-D infinite space", *Int. J. Comput. Methods*, 2141020. https://doi.org/10.1142/S0219876221410206

Schanz, M. and Antes, H. (1997), "Application of operational quadrature methods in time domain boundary element method", *Meccanica*., **32**, 179-186. http://doi.org/10.1023/A:1004258205435

Schanz, M. (2001), *Wave Propagation in Viscoelastic and Poroelastic Continua: A Boundary Element Approach*, Springer.

Shaw, I.D. and Andrawes, B. (2017), "Finite element analysis of CFRP laminate repairs on damaged end regions of prestressed concrete bridge girders", *Adv. Comput. Des.*, **2**(2), 147-168. https://doi.org/10.12989/acd.2017.2.2.147

Terada, K., Miura, T. and Kikuchi, N. (1997), "Digital image-based modeling applied to the homogenization analysis of composite materials", *Comput. Mech.*, **20**(4), 331-346. https://doi.org/10.1007/s004660050255

Von, E.O. and Prabucki, M.J. (1990), "Dynamic response in the time domain by coupled boundary and finite elements", *Comput. Mech.*, **6**, 35-46.

Xinzhong, G. and Shunming, L. (2018), "Convolution quadrature time-domain boundary element method for two-dimensional aeroacoustic noise prediction", *Acoust. Phys*, **64**, 731–741.

Yu, W., Yang, X., Liu, Y., Mittra, R. and Muto, A. (2011), *Advanced FDTD Method: Parallelization, Acceleration, and Engineering Applications*, Artech House.

CC